Soft Matter

Partitioning of Active Particles into Porous Media

Soft Matter

ARTICLE TYPE

Partitioning of Active Particles into Porous Media

Camilla M. Kjeldbjerg and John F. Brady*

Passive Brownian particles partition homogeneously between a porous medium and an adjacent fluid reservoir. In contrast, active particles accumulate near boundaries and can therefore preferentially partition into the porous medium. Understanding how active particles interact with and partition into such an environment is important for optimizing particle transport. In this work, both the initial transient and steady behavior as active swimmers partition into a porous medium from a bulk fluid reservoir are investigated. At short times, the particle number density in the porous medium exhibits an oscillatory behavior due to the particles' ballistic motion when time $t < \tau_R$, where τ_R is the reorientation time of the active particles. At longer times, $t > L^2/D^{swim}$, the particles diffuse from the reservoir into the porous medium, leading to a steady state concentration partitioning. Here, L is the characteristic length scale of the porous medium and $D^{swim} = U_0\ell/d(d-1)$, where U_0 is the intrinsic swim speed of the particles, $\ell = U_0\tau_R$ is the particles' run, or persistence, length, and d is the dimension of the reorientation process. An analytical prediction is developed for this partitioning for spherical obstacles connected to a fluid reservoir in both two and three dimensions based on the Smoluchowski equation and a macroscopic mechanical momentum balance. The analytical prediction agrees well with Brownian dynamics simulations.

1 Introduction

Active matter systems span a large range of length scales from bacteria and micromotors to schools of fish and humans moving in a crowded area [1–3]. The activity arises from particles self-propulsion by converting chemical energy to persistent mechanical motion [4]. This motion leads to interesting phenomena such as self-assembly, accumulation at boundaries, and the conversion of chemical energy into mechanical work through 'micro-gears' [5–7]. The utilization of new developments, such as active particle microrobots for drug therapy [8] and bacterial sequestering technologies [9], will depend on understanding not only the behavior of active particles in bulk but also in confined spaces and crowded environments such as porous media. How active particles partition into porous media and how to predict this behavior is the focus of this paper.

The simplest model that captures the essential physics of active particles is the active Brownian particle (ABP) model, wherein each particle translates with a swim speed U_0 in a direction $\boldsymbol{q}$ for a characteristic reorientation time τ_R; the average length they move between each reorientation is called the run, or persistence, length $\ell = U_0\tau_R$ [10]. Owing to this persistent swimming, the ABPs distribute non-homogenously near surfaces, accumulating at no-flux boundaries leading to a concentration boundary layer near solid surfaces [4,11,12].

Division of Chemistry and Chemical Engineering, California Institute of Technology, Pasadena, CA 91125 USA. E-mail: jfbrady@caltech.edu
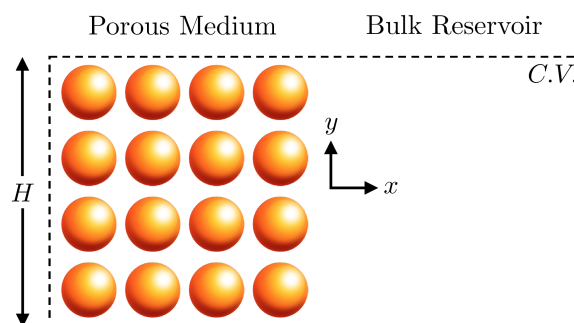
Fig. 1 Illustration of the porous medium model (i.e., an array of spheres connected to a reservoir). The obstacles are fixed, and active particles can move freely around them; further, the system is periodic in the y-direction.

In free space, the random reorientation of ABPs result in diffusive motion with $D^{swim} = U_0\ell/d(d-1)$, where d is the dimension of the reorientation process. The active swim diffusivity can be much larger than the thermal diffusivity of "passive" Brownian particles. Solid boundaries and other obstacles change the free space available to these particles and can dramatically shorten the mean-free path; this cuts off their run length, reduces the diffusivity, and causes accumulation at boundaries [11,13]. Alonso-Matilla et al. studied Taylor dispersion in circular arrays and observed, even without flow, a decrease in diffusivity for low activity particles resembling the behavior observed for passive parti-

cles[14]. Experimental studies of *Chlamydomonas Reinhardtii* show that the diffusion of algae is obstructed by arrays of pillars and becomes lower than it would be in the free space[15]. It has been shown experimentally that bacteria in a microfluidic crystal lattice (porous media) exhibit Taylor-Aris dispersion.[16] Additionally, in highly crowded environments, *E. coli* has been observed to display an interesting hopping-trapping behavior; *E. coli* is trapped in pockets of space between densely packed obstacles and then hops through highly confined channels into other pockets of pore space[17]. Chamolly *et al.* studied how activity impacts particle trajectories around a periodic lattice.[18] Further, porous media significantly impacts the chemotactic migration of bacteria as confinement strongly influences the directed motion and can cause active particles to move with the same orientation over great lengths.[19,20] Reichhardt and Reichhardt have conducted multiple studies of the effect of confinement on motility induced phase separation in dense solutions of active particles.[21,22]

Partitioning is a standard concept from thermodynamics, where Henry's law governs the concentration between two phases such that $C_A^I = K \cdot C_A^{II}$.[23,24] The partition coefficient, K, for a thermodynamic system would be determined from equality of chemical potential in the two regions, $\mu_A^I = \mu_A^{II}$. In the simplest case of hard-sphere interactions for equilibrium Brownian systems the concentration in the pore space is equal to that in the reservoir.

Even though one cannot apply the concept of a chemical potential for active matter systems, concentration distributions (or partitioning) are well understood for fundamental confining geometries such as in-, and outside a single sphere, around parallel plates in a reservoir, and channels in a wall[11,25]. However, there is a lack of knowledge regarding the partitioning of active particles for more complex environments.

This work explores both the transient and steady-state partitioning of active particles between a fluid reservoir and a porous medium (i.e., arrays of spherical obstacles). The particles interact with the obstacles through excluded volume interactions *only*. Utilizing scaling arguments relating to particle properties and geometric parameters, we explain the initial oscillations in the concentration in the bulk of the porous medium in two dimensions. We then derive a theory for the long-time partitioning between the porous medium and the reservoir in two and three dimensions based on a mechanical balance and the concentration distribution outside a single obstacle. At high activity the theory predicts

$$\frac{\langle n_{pore} \rangle}{n^\infty} = 1 + \frac{\sqrt{d}/(d-1)\,\ell/R}{1 + 1/\sqrt{d}\,\ell/R}\,\frac{\phi}{1-\phi}, \qquad (1)$$

where $\langle n_{pore} \rangle$ is the average concentration in the pore volume of the porous medium, n^∞ is the bulk concentration in the fluid reservoir, ϕ is the volume (or area) fraction of obstacles of size R in the porous medium, and ℓ is the run length. The analytical prediction agrees well with Brownian dynamics simulations. The theory and simulations suggest that a mixture of bacteria having different run lengths can be separated by contacting the solution with a porous medium whose geometric structure has a length scale $R \sim \ell$.

2   Transient evolution

We model a porous medium as an array of fixed disks (2D) on a lattice in contact with a fluid reservoir as illustrated in Fig. 1. The active particles can move in both the reservoir and in the free pore space of the porous medium. They cannot penetrate the obstacles and collide with them via excluded volume interactions. In the next section, we predict the steady-state behavior using a mechanical balance, but first we investigate the transient behavior. As previously mentioned, active particles accumulate at boundaries, and the simplest example of boundary accumulation is that of a single flat wall. Yan & Brady[11] determined that the number density n as a function of distance from the wall z at steady state is given by

$$n(z) = n^\infty \left(1 + \frac{k_s T_s}{k_B T} \exp\left(-\lambda z\right) \right), \qquad (2)$$

where $k_B T$ is the thermal energy, $k_s T_s = \zeta U_0 \ell / d(d-1)$ is the analogous active energy scale, and n^∞ is the concentration far from the wall. Here ζ is the drag coefficient of an ABP (see Appendix A). The accumulation layer decays exponentially with distance from the wall with screening length, $\lambda^{-1} = \delta/\sqrt{1 + (\ell/\delta)^2/2}$, where $\delta = \sqrt{D_T \tau_R}$ is the microscopic diffusive length and D_T is the thermal diffusivity. The ratio of the active energy scale to the thermal one can be expressed as the ratio of run length to diffusive step: $k_s T_s / k_B T = (\ell/\delta)^2/2$ in 2D[4,11].

In the porous medium, the amount of boundary available depends on the area (or volume) fraction of obstacles, $\phi = N\pi R^2/A$, where N is the number of obstacles in the total area of the porous region, A, and R is the radius of an obstacle. (The ABPs have no size. One can give them a size from the Stokes drag $\zeta = 6\pi\eta a$, where η is the fluid viscosity. In this work, the obstacle size R includes the ABP radius 'a' in its definition.) The total average number density of ABPs in the medium is defined as,

$$\langle n_{pore} \rangle = \frac{N_{ABP}}{A_f} = \frac{N_{ABP}}{A(1-\phi)}, \qquad (3)$$

where N_{ABP} is the number of ABPs in the free pore space, $A_f = A(1-\phi)$. We also define the number density outside the accumulation boundary layer as $n_{pore}^0 = N_{ABP}^*/A_f^*$, where A_f^* is the adjusted free space available excluding the area within a distance of 10 screening lengths from obstacle surfaces and N_{ABP}^* is the number of particles in A_f^*, such that only particles in the bulk pore space are included in this quantity. The inset of Fig. 8 shows the adjusted free space over which n_{pore}^0 is measured. The number density of swimmers in the reservoir is n^∞.

Both the initial and long time behavior will be set by the activity and the geometry. The inset of Fig. 4 illustrates the characteristic length scales. From dimensional analysis there are three dimensionless groups: ℓ/δ, ℓ/R, and R/L. The ratio of ℓ/δ describes the activity, ℓ/R is the ratio of particle run length to the size of an obstacle, and R/L relates to the porosity of the medium, which is also expressed as $\phi = \pi R^2/L^2$, where L is the length of one lattice unit cell. Thus, the transient evolution will be governed by these three dimensionless groups.

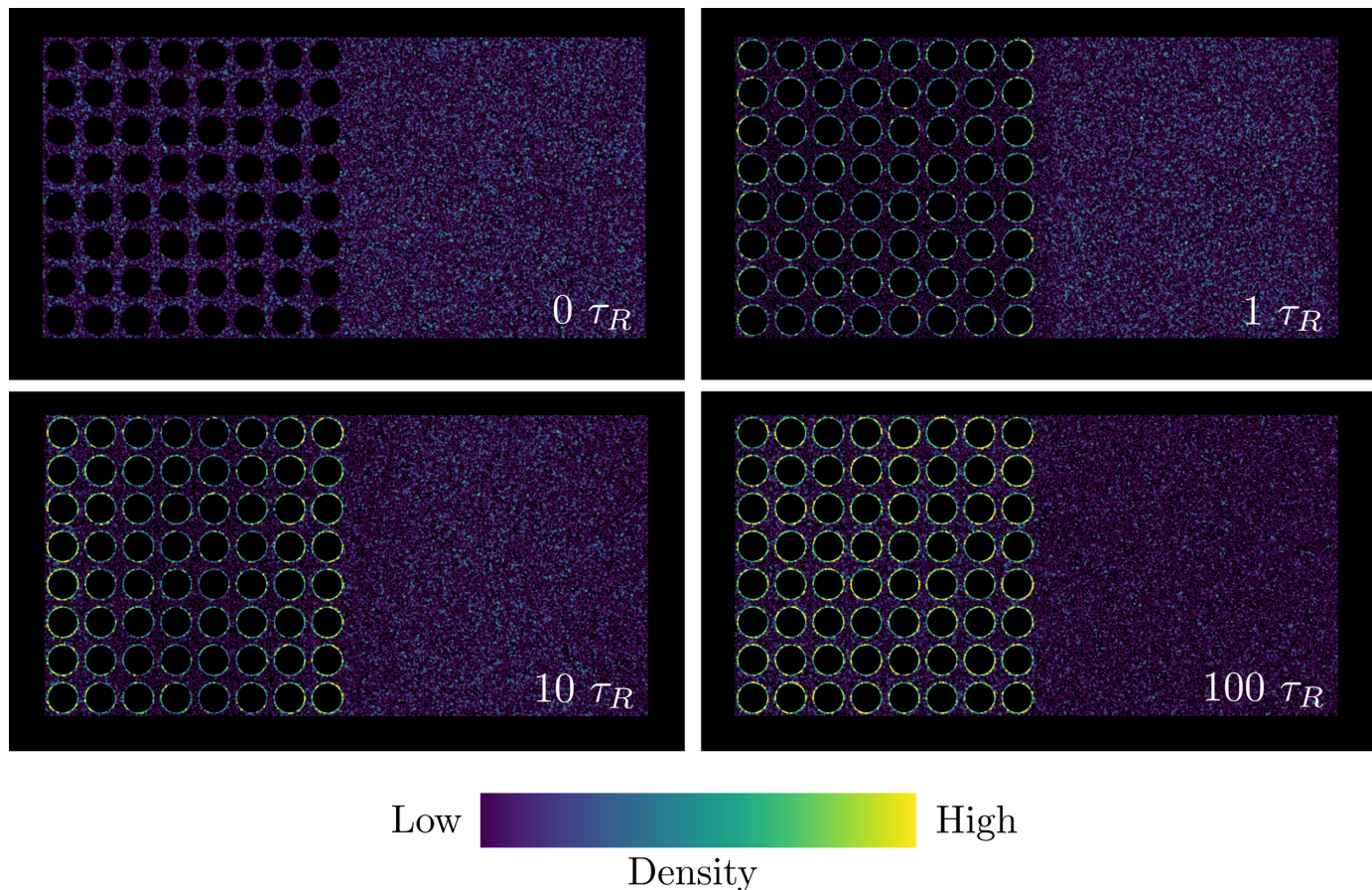The evolution of the number density for the two-dimensional

Fig. 2 Brownian dynamics simulation snapshots of particle density in the system for $k_s T_s / k_B T = 800$, $\phi = 0.5$, $\ell/R = 0.5$, and times $0\tau_R$, $1\tau_R$, $10\tau_R$, and $100\tau_R$. The circular obstacles are shown as black disks for clarity. The system is periodic in that there is an equivalent reservoir region to the left of the porous medium. Initially, the active particles are distributed homogeneously throughout the pore space and the reservoir such that the density is the same everywhere. The density within the pore space is based only on the free space available (see eq. 3). At $1\tau_R$, particles in the porous region accumulate at the obstacle surfaces, causing the concentration in the pore space to become lower than in the reservoir. At $10\tau_R$, the reservoir particles have had time to diffuse into the outer parts of the medium. Thus, the outer obstacles have a larger surface concentration than the inner obstacles, while the reservoir concentration decreases. At longer times, $100\tau_R$, the particles from the reservoir have had time to diffuse through the entire medium, and the system is near steady state.

system is shown in Fig. 2 at four times: $0\ \tau_R$, $1\ \tau_R$, $10\ \tau_R$, and $100\ \tau_R$. These results are from dilute Brownian dynamics (BD) simulations for $k_s T_s / k_B T = 800$, $\phi = 0.5$, $\ell/R = 0.5$ and 10^7 ABPs. The particles interact with obstacles through a hard-particle force, which is implemented via a potential-free algorithm[26–28]. (See Appendix A for a description of the BD simulations.) Obstacles are shown as black disks, and each active particle is color-coated with its surrounding density such that purple is low density and yellow is high density. Initially, at $0\ \tau_R$, the particles are distributed homogeneously throughout the pore space of the porous medium and the reservoir. At $1\ \tau_R$, the particles can move one run length and, as expected, particles accumulate at the obstacle surfaces leading to a lower concentration in the pore space of the porous medium compared to that in the reservoir. In Fig. 2, this is observable through the pore space of the porous medium being dark purple, while the reservoir concentration is a lighter blue. We go into more detail surrounding this lower concentration in the next section.

At $10\ \tau_R$, the particles from the reservoir have had time to diffuse into the outer edge of the porous region, where we observe a higher concentration of ABPs at the outer obstacles' surfaces, while simultaneously observing a lower concentration in the reservoir. Last, at $100\ \tau_R$, the active particles from the reservoir have had time to diffuse through the entire porous region. There are high-density boundary layers around all obstacles, while a significantly lower reservoir concentration than initially. Hence, we observe a partitioning in concentration at steady state.

In summary, two phenomena dominate the transient changes in particle concentration: 1) the persistent motion of the particles within the porous medium and 2) particles diffusing from the reservoir into the porous medium. The following sections describe these phenomena in more detail.
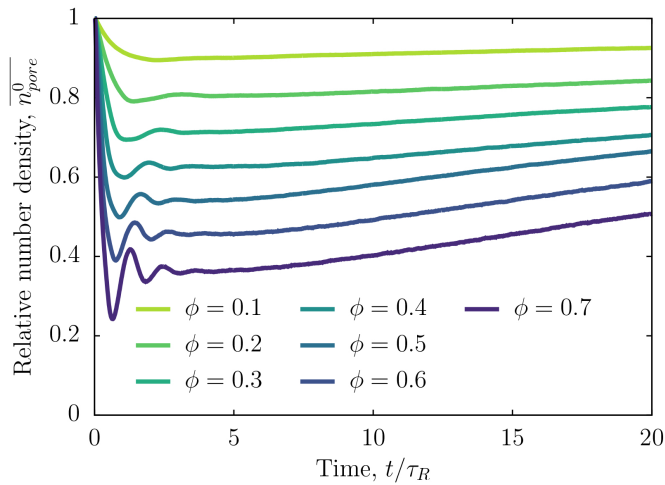
Fig. 3 Normalized number density in the pore space of the porous medium, $\overline{n_{pore}^0} = n_{pore}^0/n_{pore}^0(t = 0)$ as a function of time for $\ell/R = 0.5$, $k_s T_s/k_B T = 800$, and $\phi = 0.1 - 0.7$. The measured densities oscillate initially due to the accumulation at boundaries, when particles leave the pore space, due to their short-time ballistic nature, and then reach a temporary constant state until around a time of $5\tau_R$, after which the particles from the reservoir are diffusing into the medium and the density again increases.
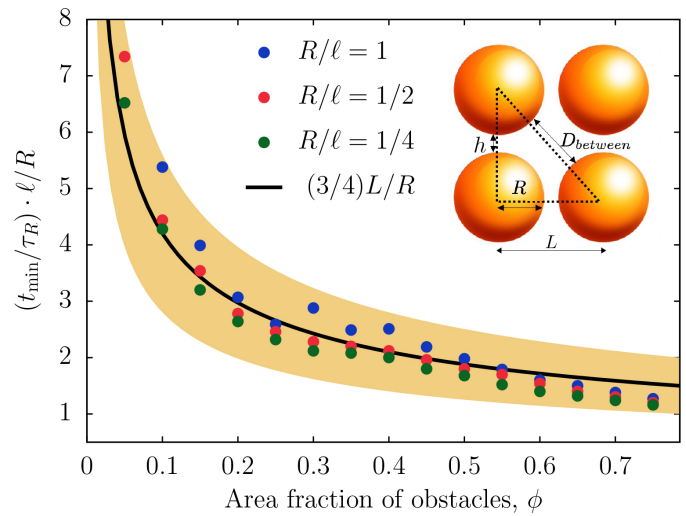

Fig. 4 Time to reach the initial local minimum in pore space concentration scaled by ℓ/R as a function of area fraction of obstacles, ϕ for $k_s T_s/k_B T = 800$ and $R/\ell = 1$, $1/2$, and $1/4$. The inset illustrates the four characteristic dimensions in the porous medium; h, R, $D_{between}$, and L. The black line corresponds to (4) with a scaling coefficient of 3/4. The gold shaded area is the interval of time between traveling an average length of $L/2$ (lower bound) and L (upper bound). At higher area fractions, the particles experience more confinement and travel a shorter distance before colliding with an obstacle than for lower area fractions.

2.1 Initial oscillations in concentration

Changes in concentration in the porous medium and the reservoir are interdependent, but initially, we can consider concentration changes in the porous medium without accounting for the effects coming from the reservoir. Particles from the reservoir require time to diffuse into the porous region, and until then the average number density in the porous medium, $\langle n_{pore} \rangle$, will be constant.

The evolution in the pore space of the porous medium, n_{pore}^0 from 0 to 20 τ_R is shown in Fig. 3. Interestingly, we initially see oscillations in the bulk number density, then a temporary constant concentration until around $5 - 10\ \tau_R$. After this, the bulk number density increases again as the reservoir particles have had time to diffuse into the porous medium. ABPs exhibit ballistic behavior at short times [29], which leads to this short-time oscillatory behavior.

We can predict when the minimum in bulk number density will occur using knowledge of this ballistic behavior. Initially, particles can move their run length and leave the pore space when they collide with an obstacle. A particle will not reenter the pore space until it reorients, which leads to a minimum in the pore space concentration. The time it takes to reach the first minimum depends on the run length of the particle compared to the length available before colliding with an obstacle, expressed through ϕ. For a given activity, a more dense system will reach the minimum faster, and this is apparent in Fig. 3. To obtain a scaling for the minimum, we use the average length a particle moves before colliding with an obstacle. At close packing or strong confinement, we expect the length to be $L/2$ on average, while for low packing fraction, we would expect that particles can move the full length, L. Thus, we estimate the minimum by the time it takes an ABP to travel the length $L = 2R + h$, where h is the shortest distance

between obstacles (as illustrated in the inset of Fig. 4);

$$\frac{t_{\min}}{\tau_R} \sim \frac{L}{\ell} \sim \sqrt{\frac{\pi}{\phi}} \cdot \frac{R}{\ell} \tag{4}$$

where $t_{\min}$ is the time to reach the minimum, τ_R is the reorientation time, and L is the length of the lattice unit cell. As mentioned, we expect the average length a particle will move before colliding to be between $L/2$ and L. Thus, we choose a scaling fit in-between the two $(3/4\ L/R)$. We compare this scaling prediction with $t_{\min}$ measured from BD simulations. The result is shown for $t_{\min}$ scaled with ℓ/R in Fig. 4, such that one can compare results for different degrees of confinement, $R/\ell = 1$, $1/2$, and $1/4$. The gold shaded area marks the interval of average travel distance between $L/2$ (lower bound) and L (upper bound). We obtain good agreement between our scaling prediction and the simulation results. As expected, near close packing or highly confined, the characteristic length to reach minimum is closer to $L/2$, while for lower confinement, the particles on average move L before reaching the minimum concentration.

Now that we have obtained a prediction for the $t_{\min}$, we can explore the number density at minimum. This will be related to the area fraction of obstacles in the medium. The larger the area fraction, the closer packed the obstacles will be and more particles will be at the boundary compared to the bulk. We propose a simple linear scaling: $n_{pore}^0(t_{\min})/n_{pore}^0(t = 0) = 1 - \alpha \cdot \phi$, where α is a constant. This leads to the behavior shown in Fig 5, where the dashed lines are linear regressions for $n_{pore}^0(t_{\min})$ computed on ϕ between 0 and 0.6. We observe linear dependence on volume fraction until near close packing.
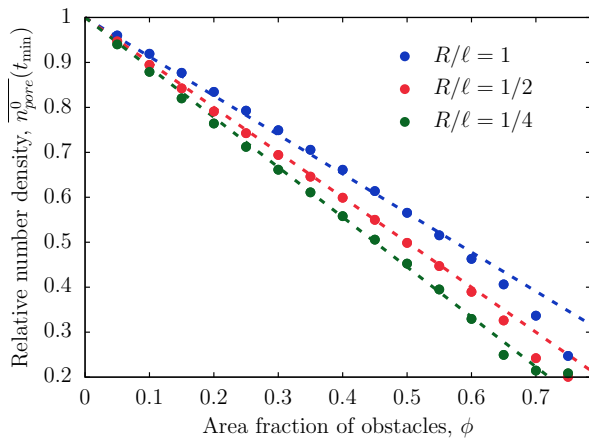
Fig. 5 The porous medium pore space number density at the initial local minimum, $\overline{n^0_{pore}(t_{\min})} = n^0_{pore}(t_{\min})/n^0_{pore}(t=0)$, as a function of area fraction of obstacles, ϕ, for $k_s T_s/k_B T = 800$ and $R/\ell = 1$, $1/2$, and $1/4$. The decrease in concentration with increased obstacle fraction is linear until near close packing. The dashed lines are linear fit to $\overline{n^0_{pore}} = 1 - \alpha\phi$ with $\alpha = 0.87$, 1 and 1.11 for $R/\ell = 1$, $1/2$ and $1/4$, respectively.

Fig. 6 Number density in the reservoir, $\overline{n^\infty} = n^\infty/n^\infty(t=0)$, as a function of time for $R/\ell = 0.5$, $k_s T_s/k_B T = 800$, and $\phi = 0.1-0.7$. We observe that the concentration decreases exponentially as particles diffuse out of the reservoir and reaches a steady state reservoir concentration after $\sim 100\tau_R$. This time corresponds to the characteristic time it would take a particle to explore the entire reservoir, $t_{char} \sim A_{res}/U_0^2\tau_R$, where A_{res} is the size of the reservoir.

2.2 Porous media as a sponge

The concentration in the center of the reservoir initially remains constant until $5\,\tau_R$, after which it rapidly decreases before reaching a steady value. The changes in reservoir concentration, n^∞, scaled by the initial concentration, $n^\infty(t=0)$, are shown in Fig. 6. The steady-state concentration in the reservoir depends on the volume fraction of the porous medium. The higher the volume fraction, the lower the reservoir concentration, even though there is less pore space in the denser porous medium! The porous medium acts as a sponge and soaks up the ABPs.

This emptying of the reservoir poses exciting opportunities for application design. Imagine a bath of active particles, such as bacteria, and wanting to remove them. One could temporarily insert a porous medium and utilize this mechanism to rapidly drain out the bacteria. With the knowledge of the area fraction dependence, one could either drain an optimal amount or achieve the maximum drainage effect by having a high area fraction of obstacles in the porous medium. One could also separate a mixture of bacteria if they had different run lengths. In the next section, we predict the long-time partitioning between the porous medium and the fluid reservoir.

3 Partitioning into a porous medium

3.1 Two dimensions

Fig. 7 shows the average number density in the porous medium, $\langle n_{pore} \rangle/n^\infty$, as a function of the area fraction of obstacles, ϕ. Passive particles distribute homogeneously independent of the system geometry. However, when the particles are active, there is an increased concentration in the porous medium compared to the reservoir at steady state. The partitioning depends on the three nondimensional parameters: ℓ/δ, ℓ/R, and ϕ. We can determine how the partitioning scales with these parameters, and analytically predict the partitioning from the governing Smoluchowski
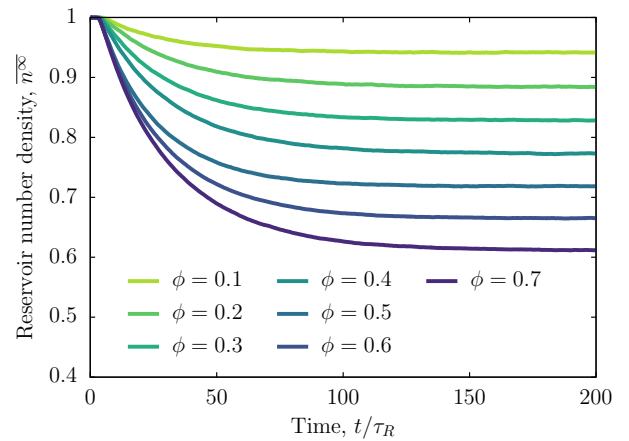
equation. First, we relate the average concentration in the porous medium $\langle n_{pore} \rangle$ to the one in the bulk pore space n^0_{pore}. For high activities, we can assume that the accumulation boundary layers are thin such that they do not overlap, and each obstacle can be viewed as isolated and surrounded by a concentration of n^0_{pore}. From the analytical expression for ABP accumulation outside a single disk, we integrate over all N obstacles within the porous medium to obtain

$$\frac{\langle n_{pore} \rangle}{n^0_{pore}} = 1 + \frac{2\pi N}{A_f} \int_R^\infty \left(\frac{n(r)}{n^0_{pore}} - 1 \right) r \, \mathrm{d}r, \qquad (5)$$

where $n(r)$ is the concentration profile outside a single disk in two-dimensions. The area fraction of obstacles is $\phi = \pi R^2 N/A$. The free space area is $A_f = A(1 - \phi)$. At high activity, the boundary layer is thin, and by subtracting the bulk concentration, we know that $n(r)/n^0_{pore} - 1$ will be confined to the accumulation layer, and we have

$$\int_R^\infty \left(\frac{n(r)}{n^0_{pore}} - 1 \right) r \, \mathrm{d}r \sim (\ell/\delta)^2 R/\lambda. \qquad (6)$$

Thus, the average concentration in the porous medium relative to that in the pore space is

$$\frac{\langle n_{pore} \rangle}{n^0_{pore}} = 1 + C_{2D}\frac{\phi}{1 - \phi}, \qquad (7)$$

where C_{2D} is a numerical factor from the 2D disk solution of Yan & Brady[11]:

$$C_{2D} = \frac{4}{\lambda R}\frac{(\ell/\delta)^2 \mathrm{K}_1(\lambda R)}{\mathrm{K}_0(\lambda R)[2 - (\ell/\delta)^2] + \mathrm{K}_2(\lambda R)[2 + (\ell/\delta)^2]}, \qquad (8)$$

where K_0 and K_2 are Bessel-functions. (See Appendix A for details on the Smoluchowski equation and statistical moments' expansion.) The analysis leading to (7) requires the accumulation

layer to be thin, $\lambda R \gg 1$, and in the high activity limit, $\ell/\delta \gg 1$, C_{2D} is independent of the microscopic length δ and takes the simple form

$$C_{2D} = \frac{\sqrt{2}\,\ell/R}{1 + \frac{1}{\sqrt{2}}\ell/R}, \tag{9}$$

when $\delta/R \ll 1$ and $\ell/\delta \gg 1$. Thus, with (7) and (9), we have a relation between $\langle n_{pore} \rangle$ and n_{pore}^0. To determine the partitioning between the porous medium and the reservoir, we still need to relate the uniform concentration in the pore space, n_{pore}^0, to the reservoir concentration n^∞.

As in our previous work for parallel plates [25], we apply a momentum balance to the control volume shown in Fig. 1, which, as discussed in Appendix B, yields

$$n_{pore}^0 = n^\infty [1 + 2\overline{Q}_{xx}^{pore}]^{-1}, \tag{10}$$

where $\overline{Q}_{xx}^{pore}$ is the nematic order density in the pore space. Assuming the nematic order is negligible, (10) reduces to

$$n_{pore}^0 = n^\infty, \tag{11}$$

where n^∞ is the bulk concentration in the reservoir and n_{pore}^0 is the pore space concentration in the porous medium. The pore space concentration in the porous medium only accounts for ABPs outside a distance of 10 screening lengths of the obstacle surfaces. The screening length is the characteristic thickness of accumulation boundary layer, λ^{-1}, and the bulk area is shown in gray in the inset of Fig. 8. We validate (11) through BD simulations, and Fig. 8 shows n_{pore}^0/n^∞ as a function of the area fraction of obstacles. When the area fraction is near close packing, our thin boundary layer approximation no longer holds, and the boundary layers overlap. However, for our range of area fractions, we observe $n_{pore}^0/n^\infty = 1$ within a 90% margin. This deviation is due to the edge effects of the porous medium and the neglect of the nematic order term in (10). The nematic order is negative at the edge of the boundary layer.

The combination (7), (9), and (11) form the analytical prediction for the partitioning confirm that the partitioning in the porous medium scales linearly as $\phi/(1-\phi)$. Fig. 9 shows the excellent comparison between our analytical prediction and the results from BD simulation. From the partitioning we can also obtain the steady state drop in reservoir concentration from the overall conservation of particle number.

3.2 Three dimensions

We predict the partitioning between a lattice of spheres in contact with a fluid reservoir in three dimensions (shown in the inset of Fig. 10) using arguments analogous to that for the two-dimensional geometry. Fig. 10 shows the value of n_{pore}^0/n^∞ as a function of the volume fraction of obstacles. As before, the prediction for the partitioning is

$$\frac{\langle n_{pore} \rangle}{n_{pore}^0} = 1 + \frac{4\pi N}{V_f} \int_R^\infty \left[\frac{n(r)}{n_{pore}^0} - 1 \right] r^2 \, \mathrm{d}r. \tag{12}$$

In three dimensions, the volume fraction is $\phi = \frac{4}{3}\pi N R^3/V$ and further reduced by $V_f = V(1-\phi)$. Equivalent to the two-
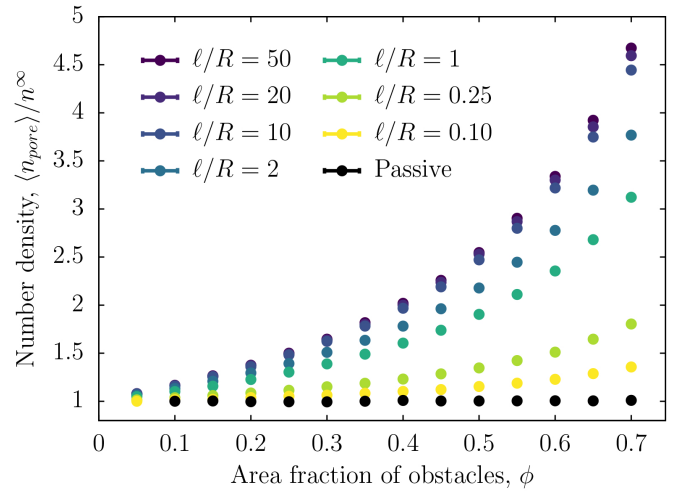

Fig. 7 Average number density in the two-dimensional porous medium, $\langle n_{pore} \rangle/n^\infty$, as a function of the area fraction of obstacles, ϕ, for ratios of obstacle size to run length, $R/\ell \in [0.1, 50]$, at steady state with activity $k_s T_s \sim 5000 k_B T$.

dimensional case, we have

$$\frac{\langle n_{pore} \rangle}{n_{pore}^0} = 1 + C_{3D} \frac{\phi}{1-\phi}, \tag{13}$$

where C_{3D} is a numerical factor from the 3D sphere solution of Yan & Brady and is given by

$$C_{3D} = \frac{\frac{1}{2}(\ell/\delta)^2(\lambda R + 1)}{1 + (1 + \lambda R)(\delta/R)^2} \frac{1}{(R\lambda)^2}. \tag{14}$$

As before, in the high activity limit where $\ell/\delta \gg 1$ and $\lambda R \gg 1$, the scaling factor becomes

$$C_{3D} = \frac{\frac{\sqrt{3}}{2}\frac{\ell}{R}}{1 + \frac{1}{\sqrt{3}}\frac{\ell}{R}}. \tag{15}$$

For high activity the scale factor depends only on the degree of confinement, ℓ/R. The combination of (13) and (14) with $n_{pore}^0 = n^\infty$ gives the full analytical prediction of the partitioning between a reservoir and a porous medium in three dimensions and is compared to results from BD simulations in Fig. 11. Notice that having $k_s T_s \sim 250 k_B T$ or $k_s T_s \sim 800 k_B T$ leads to the same partitioning independent of the two activities when the degree of confinement, ℓ/R, is the same, thus validating (15). The scaling coefficient has the general form given in (1).

4 Conclusions

The transient evolution of the number density in porous media (i.e., two-dimensional arrays of circles) shows a fascinating initial oscillatory behavior. Through dimensional analysis, we argue that the behavior only depends on the activity, the degree of confinement (ratio of run length to obstacle size), and the area fraction of obstacles. We predict this behavior when the length scales in the medium are on the order of the particle run length. After the
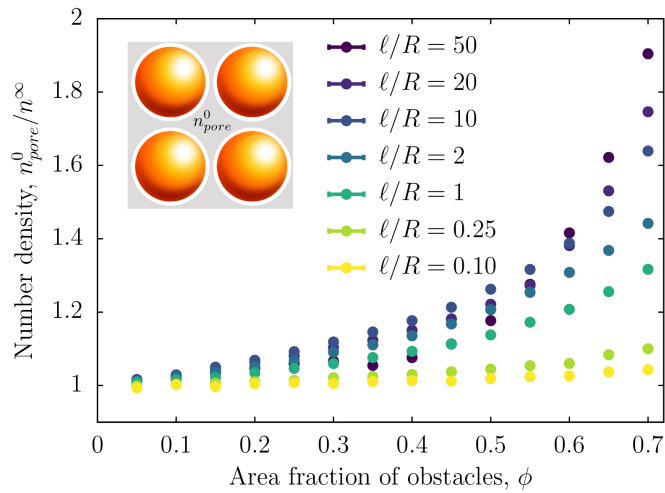
Fig. 8 Average number density in the pore space of porous medium, n^0_{pore}, to that in the reservoir, n^∞ as a function of the area fraction of obstacles, ϕ, at steady state and $k_s T_s \sim 5000 k_B T$. Inset shows the region (gray) for which n^0_{pore} is computed.

Fig. 10 Average pore space number density in the porous medium, n^0_{pore}, to that in the reservoir, n^∞ as a function of the volume fraction of obstacles, ϕ, at steady state and $k_s T_s \sim 250 k_B T$. The inset illustrates the porous medium in three dimensions (i.e., spheres on a cubic lattice in contact with a fluid reservoir).
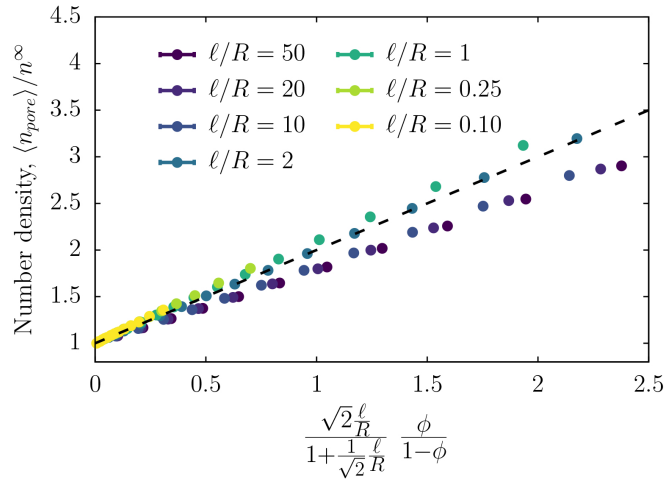

Fig. 9 Relative number density in the porous medium, $\langle n_{pore} \rangle$, to that in the reservoir, n^∞ as a function of a combination of degree of confinement, C_{2D}, and obstacle volume fraction $\phi/(1-\phi)$ leading to linear partitioning dependence at steady state in two dimensions and $k_s T_s \sim 5000 k_B T$. The dashed line show the analytical prediction in (7) combined with (11), where C_{2D} is given by (9).

initial oscillations, the particles from the reservoir diffuse into the porous medium, which decreases the concentration in the reservoir, while increasing the concentration in the porous medium, leading to a partitioning in concentration.

We presented a model for the concentration partitioning between a porous medium and external environments at steady-state, and predicted a linear dependence between the partitioning and a combination of degree of confinement and the area fraction of obstacles. The analytical prediction is determined by applying a mechanical momentum balance and utilizing the concentration profile outside a single disk/sphere (2D/3D). Our analytical prediction agrees well with results from Brownian dynamics simu-
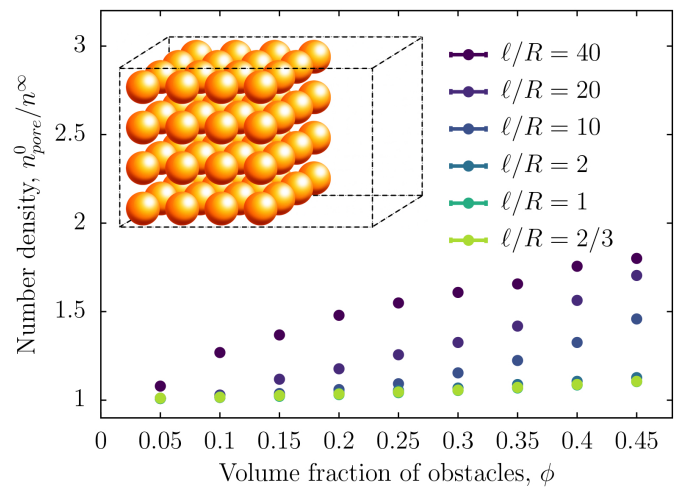
lation in both two and three dimensions. While the prediction is for a regular lattice porous medium, and many environments in nature are less structured, we expect that the general ideas and scaling should apply to disordered media. However, disordered media will create corners between obstacles, where active particles would get trapped leading to an increased partitioning. This work provides a foundation for understanding partitioning in more complex and confined environments. Additionally, our predictive model can be utilized for designing geometrical configurations of porous media that can capture a desired concentration of active particles.

A Theoretical framework

This work depends on two methods for obtaining analytical predictions and results: conservation equations and Brownian dynamics simulations. The Smoluchowski equation governs the probability, P, for finding an active Brownian particle at a specific position x with orientation q:

$$\frac{\partial P(x, q, t)}{\partial t} + \nabla \cdot j^T + \nabla_R \cdot j^R = 0, \qquad (16)$$

where the translational and rotational fluxes are: $j^T = U_0 q P + F^W P/\zeta - D_T \nabla P$ and $j^R = -D_R \nabla_R P$. Here, $\nabla_R = q \times \nabla_q$ is the orientational gradient operator, and D_T and D_R are the translational and rotational diffusivity, respectively. The number density is obtained by expanding the Smoluchowski equation in statistical moments [30], such that $n(x,t) = \int P(x, q, t) dq$, $m(x,t) = \int q P(x, q, t) dq$, which leads to the equations in 2D [30]:

$$\frac{\partial n}{\partial t} + \nabla \cdot j_n = 0, \qquad (17)$$

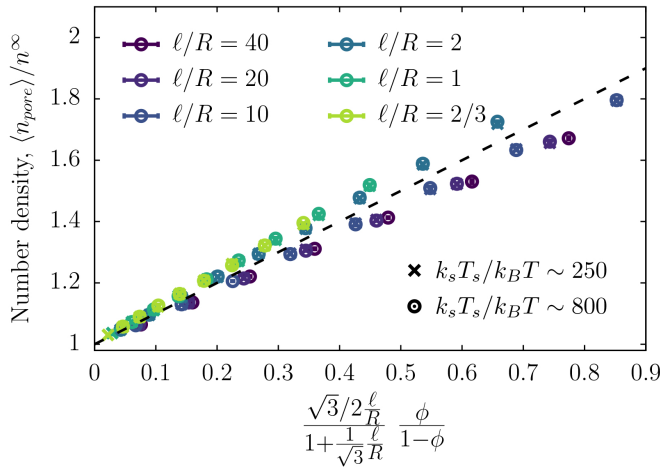$$\frac{\partial m}{\partial t} + \nabla \cdot j_m + D_R m = 0, \qquad (18)$$

Fig. 11 Relative number density in the porous medium, $\langle n_{pore} \rangle$, to that in the reservoir, n^∞, as a function of a combination of degree of confinement, C_{3D}, and obstacle volume fraction $\phi/(1-\phi)$ leading to linear partitioning dependence at steady state in three dimensions for $k_s T_s \sim 250 k_B T$ and $k_s T_s \sim 800 k_B T$. The dashed lines show the analytical prediction in (13), where C_{3D} is given by (15).

where the fluxes are given by

$$\boldsymbol{j}_n = U_0 \boldsymbol{m} - D_T \nabla n, \qquad (19)$$

$$\boldsymbol{j}_m = U_0 \boldsymbol{Q} + \frac{1}{2} U_0 n \boldsymbol{I} - D_T \nabla m, \qquad (20)$$

where n is the number density, $\boldsymbol{m}$ is the polar order, and $\boldsymbol{Q}(\boldsymbol{x}, t) = \int (\boldsymbol{qq} - \boldsymbol{I}/2) P(\boldsymbol{x}, \boldsymbol{q}, t) d\boldsymbol{q}$ is the nematic order. Assuming an isotropic nematic order, $\boldsymbol{Q} = 0$, we can close the expansion. These equations can be solved for simple geometries to obtain analytical expressions for the concentration distribution. Yan & Brady solved these equations outside a disk in two-dimensions and a sphere in three-dimensions subject to no flux at $r = R$[11]. Applying these analytical solutions of the Smoluchowki equations in combination with no net-force balances over specific control volumes in the porous medium (Appendix B), we obtain analytical predictions for the behavior.

To verify the analytical predictions, we perform Brownian dynamic simulations. These simulations can be viewed as numerically solving the particles' equation of motion: The overdamped Langevin equations[30],

$$\boldsymbol{0} = -\zeta \boldsymbol{U} + \boldsymbol{F}^{Swim} + \boldsymbol{F}^B, \qquad (21)$$

$$\boldsymbol{0} = -\zeta_R \boldsymbol{\Omega} + \boldsymbol{L}^R, \qquad (22)$$

where $\boldsymbol{U}$ is the translational velocity, $\boldsymbol{\Omega}$ is the rotational velocity, ζ_R is the rotational Stokes drag, and $\boldsymbol{F}^{Swim}$ is the swim force defined to be $\boldsymbol{F}^{Swim} \equiv \zeta U_0 \boldsymbol{q}$. $\boldsymbol{F}^B$ is the random Brownian force with the properties $\overline{\boldsymbol{F}^B} = \boldsymbol{0}$ and $\overline{\boldsymbol{F}^B(0)\boldsymbol{F}^B(t)} = 2 k_B T \zeta \delta(t) \boldsymbol{I}$, where $\boldsymbol{I}$ is the identity tensor and $\delta(t)$ is the delta-function. $\boldsymbol{L}^R$ is the random reorientation torque where $\overline{\boldsymbol{L}^R} = \boldsymbol{0}$ and $\overline{\boldsymbol{L}^R(0)\boldsymbol{L}^R(t)} = 2 \zeta_R^2 \delta(t) \boldsymbol{I}/\tau_R$. Length scales are non-dimensionalized by the microscopic length $\delta = \sqrt{D_T \tau_R}$ and the time steps are non-

dimensionalized by the reorientation time, τ_R. The orientation of the translational motion $\boldsymbol{q}$ is related to the angular velocity $\boldsymbol{\Omega}$ via: $d\boldsymbol{q}/dt = \boldsymbol{\Omega} \times \boldsymbol{q}$. The particles interact with obstacles through a no flux condition, which is implemented via a potential-free algorithm[26–28] In order to obtain steady state and minimize the impact of fluctuations and errors, the simulations are computed with $\sim 10^6$ particles and a minimum of $10^4 \tau_R$. For the transient results, the simulations are computed with $\sim 10^7$ particles.

B Momentum balance

From the macroscopic Langevin equations we can write the momentum balance

$$0 = -\zeta \boldsymbol{j}_n + \zeta U_0 \boldsymbol{m} + \nabla \cdot \boldsymbol{\sigma}^{osmo}, \qquad (23)$$

where the flux is given by $\boldsymbol{j}_n \equiv n \frac{1}{N} \sum_{\alpha=1}^N \boldsymbol{U}_\alpha$, the polar order is $\boldsymbol{m} \equiv n \frac{1}{N} \sum_{\alpha=1}^N \boldsymbol{q}_\alpha$, and $\boldsymbol{\sigma}^{osmo} = -n k_B T \boldsymbol{I}$ is the osmotic pressure. In the force balance (23) $-\zeta \boldsymbol{j}_n$ is the average drag force from the suspending medium (which is assumed to be stationary), $\zeta U_0 \boldsymbol{m}$ is the average propulsive or swim force, and since the average of the Brownian force is zero, its effect appears as the divergence of a stress $\nabla \cdot \boldsymbol{\sigma}^{osmo}$. The polar order can be written in terms of its flux as $\boldsymbol{m} = -\tau_R \nabla \cdot \boldsymbol{j}_m$, and the expression for polar order flux is given in (20). Thus, the momentum balance becomes

$$0 = -\zeta \boldsymbol{j}_n + \nabla \cdot [\boldsymbol{\sigma}^{osmo} - \zeta \ell \boldsymbol{j}_m]. \qquad (24)$$

At steady state $\nabla \cdot \boldsymbol{j}_n$ can be written as $j_i^n = \frac{\partial}{\partial x_j} j_j^n x_i$; thus, the momentum balance becomes

$$\nabla \cdot [\boldsymbol{\sigma}^{osmo} - \zeta \ell \boldsymbol{j}_m - \zeta \boldsymbol{j}_n \boldsymbol{x}] = 0. \qquad (25)$$

We apply this momentum balance to the control volume (C.V.) illustrated in Fig. 1:

$$0 = \oint \boldsymbol{n} \cdot [\boldsymbol{\sigma}^{osmo} - \zeta \ell \boldsymbol{j}_m - \zeta \boldsymbol{j}_n \boldsymbol{x}] dS, \qquad (26)$$

where $\oint [...] dS$ designates the integral over all surfaces. Integrating the x-component gives

$$0 = H[(-\sigma_{xx}^{osmo} + \zeta \ell j_{xx}^m + \zeta j_x^n x)|_L \qquad (27)$$

$$+ (\sigma_{xx}^{osmo} - \zeta \ell j_{xx}^m - \zeta j_x^n x)|_R] + \sum_P \oint \boldsymbol{n} \cdot \boldsymbol{\sigma}^{osmo} dS \cdot \boldsymbol{1}_x,$$

where subscripts L and R refer to the left and right boundary of C.V., and $\sum_P \oint [...] dS$ is the integral over all obstacles in C.V.. For the left and right boundary, we have

$$(-\sigma_{xx}^{osmo} + \zeta \ell j_{xx}^m + \zeta j_x^n x)|_L = \qquad (28)$$

$$n_{pore}^0 (k_B T + k_s T_s) + 2 k_s T_s Q_{xx}^{pore},$$

$$(\sigma_{xx}^{osmo} - \zeta \ell j_{xx}^m - \zeta j_x^n x)|_R = -n^\infty (k_B T + k_s T_s), \qquad (29)$$

where $k_s T_s = \zeta \ell U_0 / d(d-1)$. Note that the particle flux j_n^x is zero at both boundaries, thus the momentum balance in (27) becomes

$$(k_B T + k_s T_s)(n_{pore}^0 - n^\infty) + 2 k_s T_s Q_{xx}^{pore} =$$

$$\frac{1}{H} \sum_P \oint n k_B T \boldsymbol{n} dS \cdot \boldsymbol{1}_x. \qquad (30)$$

For all particles fully inside the porous medium, we know that $\int n k_B T \boldsymbol{n} dS = 0$. Even for the particles at the edge, this could be at most proportional to $n_{pore}^0 - n^\infty$. Therefore, we have that

$$\int n k_B T \boldsymbol{n} dS \cdot \boldsymbol{1}_x = \alpha (n_{pore}^0 - n^\infty) k_s T_s \pi R, \qquad (31)$$

where R is the obstacle radius and α is an unknown scaling coefficient. The contribution from the edge will depend on the number of particles at the edge within the control volume, which is $N_{edge} = H/L$, where H is the height of the control volume and L is the length of a unit cell. Thus, the momentum balance becomes

$$(k_B T + k_s T_s)\left[1 + \alpha \frac{\pi R}{L}\right](n_{pore}^0 - n^\infty)$$

$$+ 2 k_s T_s Q_{xx}^{pore} = 0. \qquad (32)$$

In the porous medium, the nematic order can be written as $Q_{xx}^{pore} = n_{pore} \overline{Q}_{xx}^{pore}$, such that

$$\left[(k_B T + k_s T_s)\left[1 + \alpha \frac{\pi R}{L}\right] + 2 k_s T_s \overline{Q}_{xx}^{pore}\right] n_{pore}^0 =$$

$$(k_B T + k_s T_s)\left[1 + \alpha \frac{\pi R}{L}\right] n^\infty. \qquad (33)$$

Or,

$$n_{pore}^0 = n^\infty \left[1 + \frac{2 k_s T_s \overline{Q}_{xx}^{pore}}{(k_B T + k_s T_s)(1 + \alpha \frac{\pi R}{L})}\right]^{-1} \qquad (34)$$

From Yan & Brady[11] we know that $\overline{Q}_{xx} < 0$ away from the obstacle surface. Hence, $n_{pore}^0 > n^\infty$ and becomes increasingly so the higher the area fraction ϕ. Assuming the edge effects are negligible α must be small, and the expression becomes

$$n_{pore}^0 = n^\infty \left[1 + \frac{2 \overline{Q}_{xx}^{pore}}{1 + k_B T / k_s T_s}\right]^{-1}, \qquad (35)$$

which for high activity ($k_s T_s \gg k_B T$) is the expression in (10).

Conflicts of interest

There are no conflicts to declare.

Acknowledgements

Notes and references

1 E. Lauga and T. R. Powers, Reports on Progress in Physics, 2009, **72**, 096601.

2 S. Granick, S. Jiang and Q. Chen, Physics Today, 2009, **62**, 68–69.

3 F. Wurm and A. F. M. Kilbinger, Angewandte Chemie-international Edition, 2009, **48**, 8412–8421.

4 S. C. Takatori and J. F. Brady, Current Opinion in Colloid and Interface Science, 2016, **21**, 24–33.

5 S. A. Mallory, C. Valeriani and A. Cacciuto, Annual Review of Physical Chemistry, 2018, **69**, 59–79.

6 C. Maggi, J. Simmchen, F. Saglimbeni, J. Katuri, M. Dipalo, F. De Angelis, S. Sanchez and R. Di Leonardo, Small, 2016, **12**, 446–451.

7 C. Bechinger, R. Di Leonardo, H. Löwen, C. Reichhardt, G. Volpe and G. Volpe, Rev. Mod. Phys., 2016, **88**, 045006.

8 W. Gao, R. Dong, S. Thamphiwatana, J. Li, W. Gao, L. Zhang and J. Wang, ACS nano, 2014, **9**, 117–123.

9 R. Di Giacomo, S. Krödel, B. Maresca, P. Benzoni, R. Rusconi, R. Stocker and C. Daraio, Scientific Reports, 2017, **7**, 1–8.

10 D. A. Beard and T. Schlick, Biophysical Journal, 2003, **85**, 2973–2976.

11 W. Yan and J. F. Brady, Journal of Fluid Mechanics, 2015, **785**, R1.

12 W. Yan and J. F. Brady, Soft Matter, 2018, **14**, 279–290.

13 S. C. Takatori, R. De Dier, J. Vermant and J. F. Brady, Nature Communications, 2016, **7**, 10694.

14 R. Alonso-Matilla, B. Chakrabarti and D. Saintillan, Physical Review Fluids, 2019, **4**, 1–21.

15 M. Brun-Cosme-Bruny, E. Bertin, B. Coasne, P. Peyla and S. Rafaï, Journal of Chemical Physics, 2019, **150**, 104901.

16 A. Dehkharghani, N. Waisbord, J. Dunkel and J. S. Guasto, Proceedings of the National Academy of Sciences of the United States of America, 2019, **166**, 11119–11124.

17 Sujit S. Datta, Soft Matter, 2019, **64**, 6545–6563.

18 A. Chamolly, T. Ishikawa and E. Lauga, New Journal of Physics, 2017, **19**, 115001.

19 T. Bhattacharjee, D. B. Amchin, J. A. Ott, F. Kratz and S. S. Datta, Biophysical Journal, 2021, **120**, 3483–3497.

20 C. Reichhardt and C. J. Reichhardt, Physical Review E, 2020, **102**, 042616.

21 C. Reichhardt and C. J. Reichhardt, Physical Review E, 2021, **103**, 062603.

22 C. Reichhardt and C. J. Reichhardt, Physical Review E, 2021, **103**, 022602.

23 W. Henry, Philosophical Transactions of the Royal Society of London, 1803, **93**, 29–274.

24 R. M. Rosenberg and W. L. Peticolas, Journal of Chemical Education, 2004, **81**, 1647–1652.

25 C. M. Kjeldbjerg and J. F. Brady, Soft Matter, 2021, **17**, 523–530.

26 D. M. Heyes and J. R. Melrose, Journal of Non-Newtonian Fluid Mechanics, 1993, **46**, 1–28.

27 W. Schaertl and H. Sillescu, Journal of Statistical Physics, 1994, **74**, 687–703.

28 D. R. Foss and J. F. Brady, Journal of Rheology, 2000, **44**, 629–651.

29 A. R. Dulaney and J. F. Brady, _Phys. Rev. E_, 2020, **101**, 052609.

30 D. Saintillan and M. J. Shelley, _Complex Fluids in Biological Systems_, Springer, 2015, ch. 9, pp. 319–355.